

# The fracture toughness of a cordierite square lattice

I. Quintana-Alonso<sup>a</sup>, S.P. Mai<sup>a</sup>, N.A. Fleck<sup>a,\*</sup>, D.C.H. Oakes<sup>b</sup>, M.V. Twigg<sup>b</sup>

<sup>a</sup> Cambridge University Engineering Department, Trumpington Street, Cambridge CB2 1PZ, UK

<sup>b</sup> Orchard Laboratories, Johnson Matthey Plc, Orchard Road, Royston SG8 5HE, UK

Received 14 July 2009; accepted 31 August 2009

Available online 6 October 2009

## Abstract

A single-edge-notch bend test was developed for the measurement of fracture toughness of a  $\pm 45^\circ$  square lattice made from an elastic-brittle solid. The finite element method was used to obtain the  $K$ -calibration for an orthotropic elastic solid, with elastic constants equal to that of the  $\pm 45^\circ$  square lattice. Finite element simulations were also used to predict the fracture strength of the cracked lattice, with failure dictated by the tensile strength of the cell-wall material. The conditions for  $K$ -dominance and for failure by a net-section strength criterion of the specimen were thereby determined. A set of fracture tests on single-edge-notch bend specimens made from the ceramic cordierite validate the predictions. The measured fracture toughness of the cordierite lattices scales linearly with the stockiness of the lattice.

© 2009 Published by Elsevier Ltd. on behalf of Acta Materialia Inc.

**Keywords:** Finite element analysis; Fracture toughness; Lattice materials; Ceramics; Toughness test

## 1. Introduction

There is increasing interest in the development of ceramic lattice materials for multifunctional application ranging from liquid–metal filters to the support structure for satellite mirrors. A prototypical example is cordierite square honeycomb, as used in the catalytic converters and diesel filters of automobiles. These lattices are creep-resistant, chemically stable and possess a high surface area to volume ratio. However, their damage tolerance is of concern as they behave in an elastic-brittle manner and are subjected to high thermal stresses in service [1,2].

Quintana and Fleck [3] have recently addressed the defect tolerance of a square honeycomb plate under remote tension containing a central crack of length  $2a$ . They found that no  $K$ -field exists at sufficiently short crack length; in this regime, the net-section tensile strength of the plate  $\sigma_{cr}$  is comparable to the unnotched strength  $\sigma_u$ , which is related to the tensile strength of the cell-wall material  $\sigma_{TS}$  by

$$\sigma_u = \frac{2}{3} \left( \frac{t}{l} \right)^2 \sigma_{TS} \quad (1)$$

where  $t$  is the cell-wall thickness and  $l$  is the cell size. Quintana and Fleck [3] also considered the net-section strength at long crack length. Then, the tensile strength is given by the linear elastic fracture mechanics (LEFM) prediction,  $\sigma_{cr} = K_{IC} / \sqrt{\pi a}$ , where the macroscopic fracture toughness  $K_{IC}$  scales linearly with stockiness  $t/l$  according to

$$K_{IC} = 0.44 \left( \frac{t}{l} \right) \sigma_{TS} \sqrt{l} \quad (2)$$

They thereby identified a transition flaw size  $a_T$  of magnitude

$$a_T = 0.14 l^3 / t^2 \quad (3)$$

such that for  $a < a_T$ , the tensile strength is given by Eq. (1) while for  $a > a_T$ , the tensile strength is given by the LEFM prediction  $\sigma_{cr} = K_{IC} / \sqrt{\pi a}$ . A major aim of the present study is to determine theoretically and experimentally the transition in behaviour from net-section strength to LEFM-control for a cracked lattice beam in bending. The single-edge notched bend (SENB) specimen is a common test geometry for fracture toughness determination.

\* Corresponding author. Tel.: +44 0 1223 748240; fax: +44 0 1223 332662.

E-mail address: [nafl@cam.ac.uk](mailto:nafl@cam.ac.uk) (N.A. Fleck).

It is usually loaded in three-point bending or in four-point pure bending, as shown in Fig. 1. Both types of loading are considered herein.

### 1.1. Outline of study

In the present study, we use the finite element method in order to predict the bending strength of a single-edge-notched bending (SENB) specimen made from an elastic-brittle,  $\pm 45^\circ$  square lattice (as sketched in Fig. 2). First, the LEFM regime is explored, and a  $K$ -calibration is obtained for the SENB specimen upon treating the lattice as an orthotropic elastic solid. The bend strength is also estimated by assuming that the crack induces no stress concentration. Second, these estimates are compared with the finite element simulations of the fracture response of the explicit cracked lattice. A test method is thereby developed for the mode I fracture toughness of the lattice. Conditions are established for  $K$ -dominance and for failure by a net-section strength criterion. Finally, the fracture toughness of a cordierite square lattice is measured for selected values of stockiness, and is compared with the numerical predictions.

## 2. $K$ -calibration for an orthotropic bend specimen

The  $\pm 45^\circ$  square lattice is orthotropic in its in-plane elastic response and this modifies the  $K$ -calibration for a SENB specimen. Finite element calculations are used to obtain the  $K$ -calibration for an elastic solid with orthotropic properties equal to that of the square lattice. The results are presented in terms of the orthotropic parameters outlined by Suo [4]. Following Suo [4], we define two non-dimensional elastic parameters

$$\lambda = \frac{A_{11}}{A_{22}}, \quad \rho = \frac{2A_{12} + A_{66}}{2\sqrt{A_{11}A_{22}}} \quad (4)$$

where  $A_{ij}$  are the compliances of the lattice as defined in Appendix A. In terms of the conventional engineering

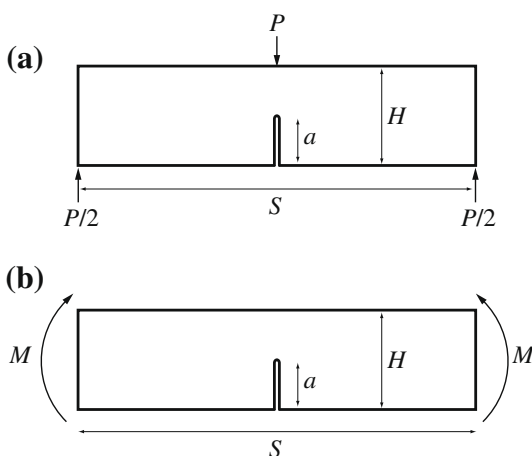


Fig. 1. Single-edge notched specimen subjected to (a) three-point bending and (b) pure bending.

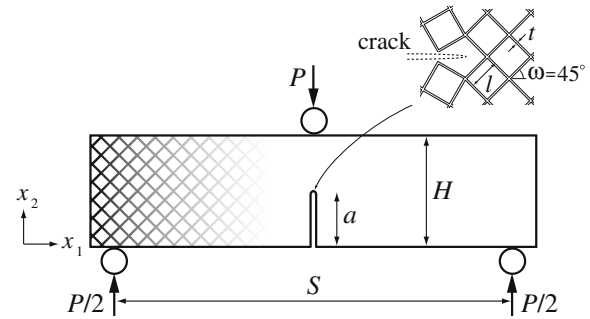


Fig. 2. Single-edge notched bend (SENB) lattice loaded in three-point bending.

moduli, the two dimensionless quantities can be expressed as

$$\lambda = \frac{E_2}{E_1}, \quad \rho = \frac{(E_1 E_2)^{1/2}}{2G_{12}} - (v_{12} v_{21})^{1/2} \quad (5)$$

These parameters measure the in-plane orthotropy. Note that  $\lambda = \rho = 1$  for isotropic materials, and  $\lambda = 1$  for materials with cubic symmetry. The requirement of positive energy density for all strain states implies that  $\lambda > 0$  and  $\rho > -1$ . For the  $\pm 45^\circ$  square lattice of the present study,  $\lambda$  equals unity and  $\rho$  is given in terms of the stockiness  $t/l$  of the lattice as (Appendix A)

$$\rho = \frac{3(t/l)^2 - 1}{(t/l)^2 + 1} \quad (6)$$

In general, the stress intensity factor for the SENB specimen depends upon geometry, and upon material orthotropy as parameterized by  $\lambda$  and  $\rho$ . Bao et al. [5] show that the effect of  $\lambda$  is negligible when  $\lambda^{1/4} S/H \geq 4$ , where  $S$  and  $H$  are the span and depth of the specimen, respectively. The stress intensity factor for a SENB specimen takes the form [5]:

$$K_I = \sigma \sqrt{\pi a} Y(\rho) F(a/H) \quad (7)$$

where  $\sigma$  is the bending stress and the dimensionless function  $Y(\rho)$  accounts for the degree of orthotropy. The geometrical factor  $F(a/H)$  is the same as that for an isotropic material, as given by Tada et al. [6]. Finite element analysis is now used to determine the dimensionless function  $Y(\rho)$  for the SENB specimen.

### 2.1. Calibration of the stress intensity factor for the orthotropic $\pm 45^\circ$ square lattice

The ABAQUS (version 6.7-1) finite element program was used to obtain the calibration factor  $Y(\rho)$  for a SENB specimen made from an orthotropic solid. The coefficients of the compliance matrix are equal to those of the  $\pm 45^\circ$  square lattice (Appendix A). Two-dimensional plane strain simulations were performed on a mesh constructed from 4-noded quadrilateral elements (type *CPE4R* in ABAQUS notation) with reduced integration.

The limit  $\rho \rightarrow -1$  is achieved by  $\nu_{12} = \nu_{21} \rightarrow 1$  and  $(E_1 E_2)^{1/2} / G_{12} \rightarrow 0$ , see Eq. (4). The solid becomes incompressible within the plane, and plane strain locking of finite elements is problematic. Strain locking was avoided in the present study by making use of elements with reduced integration and by orienting the mesh along the shear-compliant material directions of the lattice. These are at  $\pm 45^\circ$  to the  $x_1$  direction, see Fig. 2. The stress intensity factor was then extracted via the virtual crack extension method within ABAQUS.

The calibration is performed for the practical choice of geometry  $a/H = 1/2$ . Results are shown in Fig. 3a for  $\rho$  in the range  $-1 < \rho \leq 4$ . For  $\rho \geq 0$  the calibration function  $Y$  is close to unity, and there is little effect of orthotropy upon the stress intensity factor. In contrast, for  $-1 < \rho < 0$  the calibration function is sensitive to the value of  $\rho$ . The relation given by Bao et al. [5] for pure bending of a SENB specimen is included in Fig. 3a, and deviates from that of the present analysis. The reason for the discrepancy is unclear.

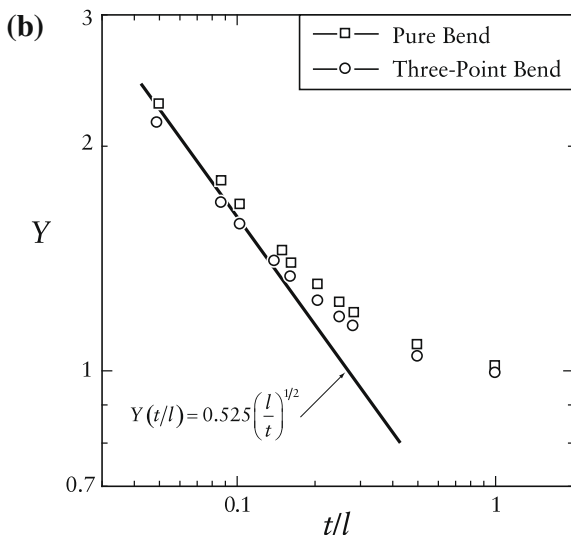
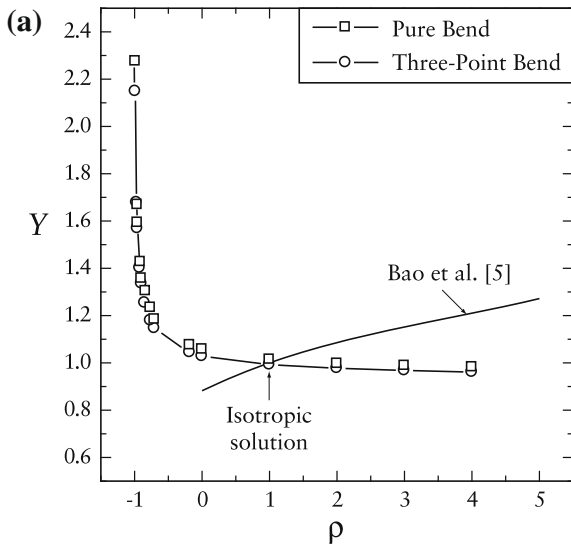


Fig. 3. Calibration function  $Y$  for the stress intensity factor of a single-edge notched specimen. The calibration is performed for  $a/H = 1/2$ .

The calibration factor  $Y(\rho)$  has been re-plotted in Fig. 3b as a function of the stockiness of the lattice  $t/l$ , by making use of relation (6). A regression analysis reveals that, for the practical range of  $t/l < 0.2$ , the factor  $Y(t/l)$  can be adequately fitted by the single function:

$$Y(t/l) = 0.525 \left( \frac{l}{t} \right)^{1/2} \quad (8)$$

for both three-point bending and pure bending, over the range  $0.05 < t/l < 0.2$ .

In summary, the stress intensity factor of the notched specimen may be obtained by first employing the calibration function  $F(a/H)$  for an isotropic material [6] and then multiplying by  $Y(\rho)$  as given by Eq. (8).

### 2.2. Prediction of the critical stress

The above  $K$ -calibration can be used to predict the critical bending stress  $\sigma_{cr}$  for fracture initiation of the elastic-brittle lattices containing a single-edge-notch. Failure occurs when the stress intensity factor  $K_I$  attains the fracture toughness of the lattice  $K_{IC}$ , as given by Eq. (2). Substitution of Eqs. (2) and (8) into Eq. (7) leads to

$$\sigma_{cr} = 0.32 \left( \frac{t}{l} \right)^{3/2} \left( \frac{l}{a} \right)^{1/2} \sigma_{TS} \quad (9)$$

for the choice  $a/H = 1/2$ . Now normalize the strength  $\sigma_{cr}$  by the unnotched strength  $\sigma_u$  of the lattice, as specified in Eq. (1), to obtain

$$\frac{\sigma_{cr}}{\sigma_u} = 0.48 \left( \frac{at}{l^2} \right)^{-1/2} \quad (10)$$

This analytical prediction is plotted in Fig. 4.

Additional finite element calculations of the  $K$ -calibration for a SENB specimen in pure bending have been

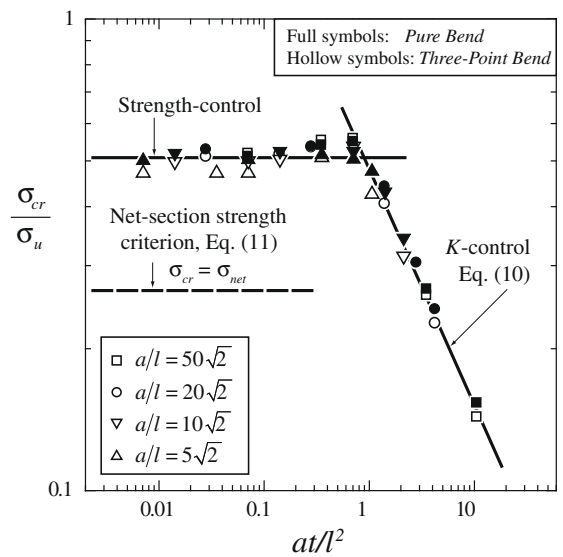


Fig. 4. Critical stress for the lattice in a SENB test. Calculations are carried out for fixed  $S/H = 5$  and  $a/H = 1/2$ .

performed; it was found that the difference in  $K$ -calibration between pure bending and three-point bending is negligible. It is emphasized, however, that it is valid for the ratio  $a/H = 1/2$ , since the  $K$ -calibration has been conducted only for this value.

### 2.2.1. The notch insensitive regime

At short crack lengths, it is anticipated that no  $K$ -field exists and the bending strength is closely related to the unnotched strength. Recall that this behaviour has already been noted by Quintana and Fleck [3] for a centre-cracked square honeycomb plate under remote tension. In the strength-controlled regime, a net-section strength criterion would suggest that the bending stress at failure  $\sigma_{net}$  is related to the unnotched bending strength  $\sigma_u$  via

$$\sigma_{cr} = \sigma_{net} = \left(1 - \frac{a}{H}\right)^2 \sigma_u = \frac{2}{3} \left(\frac{t}{l}\right)^2 \left(1 - \frac{a}{H}\right)^2 \sigma_{TS} \quad (11)$$

For the choice  $a/H = 0.5$ , this strength criterion reduces to  $\sigma_{cr}/\sigma_u = 1/4$  and this prediction has been added to Fig. 4. A transition in behaviour is predicted from notch-insensitive behaviour to the LEFM limit with increasing crack length. We proceed to confirm or refute the above predictions for the effective medium by calculating directly the bend strength of a SENB specimen, with the microstructure of a square lattice modelled explicitly.

### 2.2.2. Fracture of a discrete $\pm 45^\circ$ square lattice

A series of FE calculations on a SENB specimen made from the discrete  $\pm 45^\circ$  square lattice have been performed to validate Eqs. (10) and (11). Each strut in the lattice was modelled by an Euler–Bernoulli beam element (type *B23* in ABAQUS notation). The crack was introduced by splitting the joints along the cracking plane but with the struts on either side intact (see the sketch in Fig. 2). The magnitude of the macroscopic, critical bending stress  $\sigma_{cr}$  on the outermost fibre of the bend specimen is such that the maximum tensile stress within any strut of the lattice attains the cell-wall strength  $\sigma_{TS}$ . The resulting dependence of  $\sigma_{cr}/\sigma_u$  upon  $at/l^2$  is included in Fig. 4, for fixed  $a/H = 1/2$ . (Recall that the unnotched bend strength  $\sigma_u$  has already been defined in terms of  $\sigma_{TS}$  via Eq. (1), and this is a convenient measure for normalization of  $\sigma_{cr}$ .) Numerical results are given for specimens of increasing dimension in relation to the cell size  $l$ , as parameterized by the crack length ratio  $a/l$ . For each value of  $a/l$ , the stockiness  $t/l$  was varied from 0.001 to 0.15. The geometrical ratio  $S/H$  was held constant at  $S/H = 5$ .

Excellent agreement is noted between the predicted strength of the explicit, discrete lattice and the LEFM limit at long crack lengths. At short lengths the bend strength is independent of crack length and has a value  $\sigma_{cr}/\sigma_u$  which is half the unnotched strength but twice the net-section value. The presence of the notch degrades the bending strength by a factor of two rather than the factor of four of criterion (11). This strengthening feature is attributed to an elastic constraint effect, somewhat analogous to the plastic con-

straint in the bending of a deep-notched rigid ideally plastic solid; for this solid, the bend strength is 25% greater than the net-section strength value [7].

### 2.3. Transition crack length for $a/H = 1/2$

A simple analytical estimate can be made for the transition crack length  $a_T$  at which the failure load of the notched lattice switches from the strength-control value  $\sigma_u/2$  to the LEFM value given by Eq. (10). The transition length scales linearly with the slenderness ratio  $l/t$  according to

$$\frac{a_T}{l} \approx 0.9 \frac{l}{t} \quad (12)$$

In contrast, the transition crack length for a centre-cracked plate subjected to uniaxial tension scales as  $a_T/l \approx 0.14(l/t)^2$ , see Ref. [3]. Thus, for a slender lattice of say  $t/l = 0.01$  we have a long transition crack length  $a_T = 1400l$  in the centre-cracked plate, whereas  $a_T = 90l$  in the SENB test. Smaller specimens thereby suffice for the SENB geometry as a fracture toughness test method.

Huang and Chiang [8] carried out a numerical study of the  $\pm 45^\circ$  square lattice for both the SENB specimen in three-point bending, and the centre-cracked plate under uniaxial tension. The authors suggested that the fracture toughness measured from a three-point bend test is higher than that measured from a uniaxial test, and that the difference between the two measures is reduced as stockiness increases. This conclusion is inconsistent with the fact that the fracture toughness is a material property independent of test geometry. The paradox is resolved by the fact that most of their data lie in the strength-control regime.

## 3. Measurement of fracture toughness of cordierite square lattice

The fracture toughness of a  $\pm 45^\circ$  square lattice made from cordierite ( $2\text{MgO}-2\text{Al}_2\text{O}_3-5\text{SiO}_2$ ) is investigated by the three-point bend test, as sketched in Fig. 2. These ceramic lattices are widely used in catalytic converter applications and were supplied by Johnson Matthey Plc. Five values of the cell dimension were employed, as summarized in Table 1.

Machining and surface preparation of specimens is a critical factor in testing lattices made from porous ceramics. The specimens were hand-cut with a hacksaw, and then carefully sanded. Steel rollers of diameter 19 mm were used to support the specimen and apply the load. PTFE sheets of thickness 1 mm were placed between the rollers and the loaded faces of the specimen to reduce contact stresses. The top roller was driven at a displacement rate<sup>1</sup> of  $8 \times 10^{-3} \text{ mms}^{-1}$  by a screw-driven test machine.

<sup>1</sup> This speed of the cross-head ensures that the strain rate is below  $10^{-4} \text{ s}^{-1}$ , as required by the standard ASTM E399 [9] for quasi-static loading.



Table 1

Cell dimensions of the five batches tested in the present study. Transition crack lengths  $a_T$  calculated from Eq. (12) are valid for  $a/H = 1/2$ .

Batch	$t$ (mm)	$l$ (mm)	$t/l$	$a/l$	$a_T/l$
A	0.203	1.260	0.161	8.5	5.6
B	0.203	1.455	0.140	8.5	6.4
C	0.152	1.262	0.121	8.5	7.4
D	0.127	1.459	0.087	8.5, 11.3	10.3
E	0.051	1.035	0.049	8.5	18.4

For each batch of Table 1, eight initially undamaged specimens were tested, as well as eight specimens containing an initial edge notch of dimension  $a/H = 1/2$ . In all tests, the span to height ratio was kept constant at  $S/H = 4$ , and the thickness of the specimens was approximately 20 mm. The specimens were of height  $H$  equal to 12 cells for all batches. Additionally, for batch D, a larger specimen of height  $H$  equal to 16 cells was also tested.

The mean value and range in strength for each batch is plotted as a function of the dimensionless geometric group  $at/l^2$  in Fig. 5. The critical bending stress obtained from the notched tests  $\sigma_{cr}$  has been normalized by the average failure stress of the unnotched tests  $\sigma_u$ . Note that this critical stress is the macroscopic flexural strength of the specimen: it is related to the critical three-point bend load  $P_{cr}$  via  $\sigma_{cr} = 3P_{cr}S/2H^2$ , per unit thickness of the specimen.

Two regimes of behaviour are evident, see Fig. 5. At large values of  $at/l^2$  the critical stress is toughness-controlled: linear elastic fracture mechanics (LEFM) applies and the dependence of  $\sigma_{cr}/\sigma_u$  upon  $at/l^2$  supports the LEFM prediction (10), along with Eqs. (1) and (2). At low values of  $at/l^2$ , the failure stress of the lattice  $\sigma_{cr}$  is strength-controlled: it is insensitive to crack length and stockiness, and is approximately equal to  $\sigma_u/2$ , for the ratio  $a/H = 1/2$  considered in the experiment. These data support the FE prediction of the previous section for the limit of short crack length.

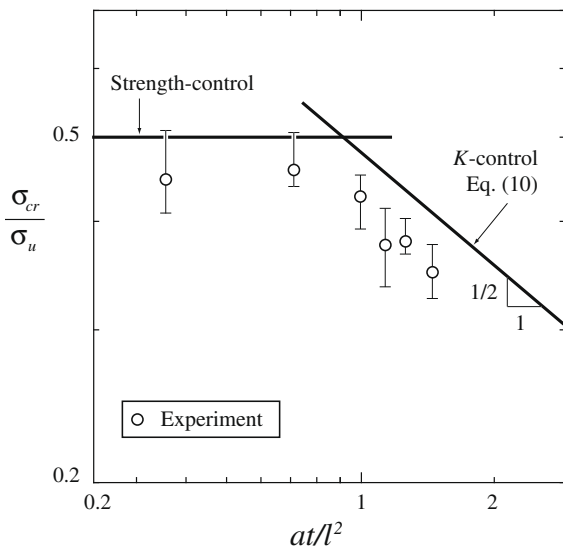


Fig. 5. Measured failure stress for a cracked lattice made from cordierite and subjected to three-point bending.  $S/H = 4$  and  $a/H = 1/2$ .

Optical images of the failed specimens are shown in Fig. 6 for an initially undamaged lattice and for a lattice containing an initial notch, both from batch A. For the undamaged lattice (Fig. 6a), failure initiates at the bottom layer of cells at about the mid-span of the specimen (where tensile stresses are highest). Struts fail successively forming a crack which propagates parallel to the loading direction, but kinks into a 45° angle before reaching the top layer of cells. For the notched lattice (Fig. 6b), the most heavily loaded struts at the crack tip fail first. The crack then propagates at 45° with respect to the loading direction. This is consistent with the fact that the  $\pm 45^\circ$  square lattice is weak in shear along these directions.

**4. Fracture toughness of cordierite lattice and tensile strength of the cell walls**

Valid  $K_{IC}$  data are summarized in Table 2 for batches A, B, and C, as well as for the specimens of batch D tested with a long notch,  $a/l = 11.3$ . Average values are given, together with their standard deviation. Batch E was only

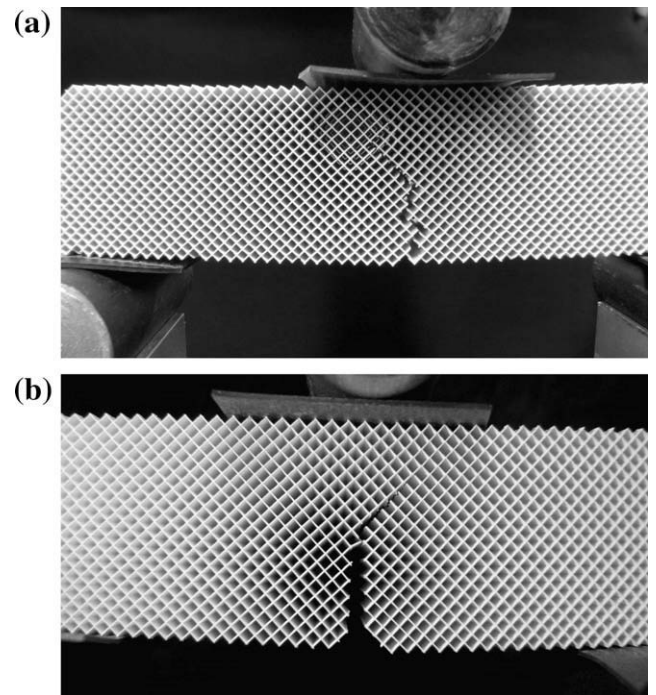


Fig. 6. Optical images of broken specimens for (a) an initially unnotched lattice and (b) a lattice containing an initial notch. Batch A of material.

Table 2

Measured tensile strength of the porous cordierite cell walls and fracture toughness of the cordierite lattice. Batch E was not tested in the  $K$ -control regime.

Batch	$K_{IC}$ (kN m <sup>-3/2</sup> )	$\sigma_{TS}$ (MPa)
A	102.7 ± 7.2	45.0 ± 0.7
B	88.7 ± 3.1	43.5 ± 1.1
C	68.6 ± 6.5	41.6 ± 1.0
D	62.3 ± 3.9	50.5 ± 3.6
E	–	148.2 ± 13.8

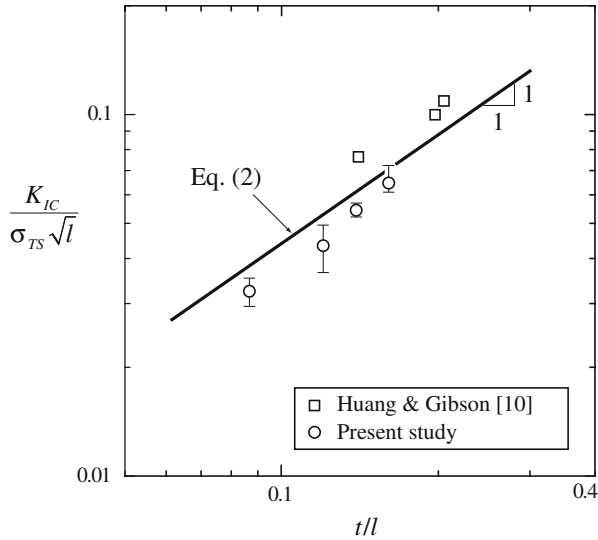


Fig. 7. Fracture toughness versus stockiness for a  $\pm 45^\circ$  square lattice made from cordierite. The error bars indicate the range of the data.

tested in the strength-control domain, see Fig. 5 and Table 1.

The tensile fracture strength  $\sigma_{TS}$  of the cell-wall material can be estimated from the failure stress measured in the unnotched tests by using Eq. (1). Average values and standard deviations are included in Table 2. It is noted that  $\sigma_{TS}$  for batch E is about three times larger than for all other batches. This is attributed to the much lower porosity of the cell-wall material for batch E, and it is consistent with the observations of Huang and Gibson [10].

The measured fracture toughness  $K_{IC}$  is plotted against stockiness  $t/l$  in Fig. 7. It is normalized by the average measured tensile strength  $\sigma_{TS}$  of the cell-wall material and the square root of the cell size  $\sqrt{l}$ . Data obtained by Huang and Gibson [10] for similar cordierite specimens have been re-calibrated employing Eq. (8) and added to Fig. 7. A comparison is made between the experimental results and the analytical prediction of Eq. (2). The experimental data follow the linear dependence upon  $t/l$  exhibited by Eq. (2). Good agreement is achieved, with most of the data lying within 15% of the analytical prediction.

#### 4.1. Prediction of fracture toughness of the lattice from the fracture toughness of cell-wall material

The cordierite lattices of the present study possess porous cell walls as a result of the extrusion and sintering of a fine ceramic paste<sup>2</sup>. This is evident in the electron micrographs shown in Fig. 8 for a cordierite lattice obtained from an automotive catalytic converter. It is important to distinguish between the material properties of the dense

<sup>2</sup> A paste is a viscoplastic formable body of dispersed particles in a polymer solution. Ceramic and glass lattices can be made by extruding a paste through a die, and then firing at high temperatures. The process is an effective way to mechanically create porosity, which is beneficial to the fabrication of porous cordierite for catalytic converter applications.

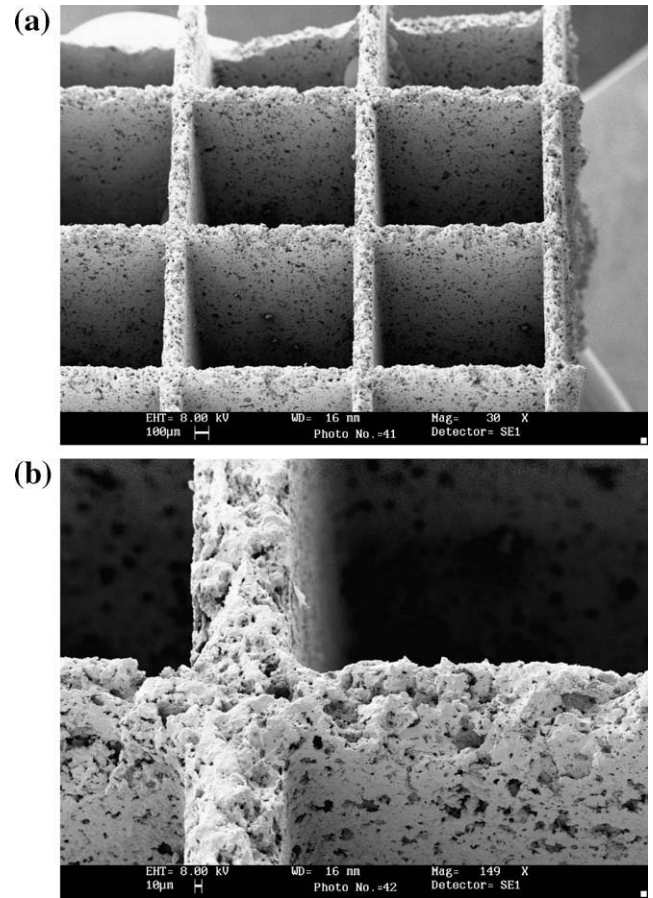


Fig. 8. Scanning electron micrographs of the cell walls of a square-celled cordierite lattice used in an automotive catalytic converter.

solid parent material, of the porous cell wall, and of the lattice structure.

The results presented above give the fracture toughness of the lattice  $K_{IC}$  in terms of the tensile strength  $\sigma_{TS}$  of the porous cell-wall material. In turn,  $\sigma_{TS}$  derives from the fracture toughness  $K_S$  of the cell wall and the intrinsic flaw size  $c$  within the cell walls

$$\sigma_{TS} \approx \frac{K_S}{\sqrt{\pi c}} \quad (13)$$

where  $c$  is the defect size within the cell wall. Substitution of Eq. (13) into Eq. (2) gives

$$\frac{K_{IC}}{K_S} = 0.23 \left( \frac{t}{l} \right) \left( \frac{l}{c} \right)^{1/2} \quad (14)$$

An estimate of the fracture toughness of the lattice  $K_{IC}$  can be obtained from Eq. (14). Values found in the literature for porous cordierite indicate  $K_S \approx 500 \text{ kN m}^{-3/2}$  for about 40–50% porosity [11,12]. The micrographs shown in Fig. 8 reveal the existence of flaws as large as  $c \approx 40 \mu\text{m}$ . Consider, for example, batch A of the present study, for which  $t = 203 \mu\text{m}$  and  $l = 1260 \mu\text{m}$ . Substitution of these values into Eq. (14) gives  $K_{IC} \approx 103 \text{ kN m}^{-3/2}$ , which is in excellent agreement with the experimental value of  $K_{IC} \approx 103 \text{ kN m}^{-3/2}$  obtained in the current study.

This alternative presentation of the fracture toughness  $K_{IC}$  has an important practical implication: improved processing techniques will reduce the intrinsic flaw size  $c$  within the cell walls, and will thereby lead to an enhanced toughness of the lattice.

## 5. Concluding remarks

The evaluation of the fracture toughness of a  $\pm 45^\circ$  square lattice from single-edge notched bend (SENB) tests requires a minimum crack length in order to ensure  $K$ -dominance at the crack tip. Finite element calculations predict that the minimum crack length is approximately given by  $a_T \approx l^2/t$ . Below this transition value, the fracture criterion switches from  $K$ -control to strength-control. Measurements on cordierite lattices confirm the existence of this transition, and the linear dependence of fracture toughness  $K_{IC}$  upon stockiness  $t/l$  for the  $\pm 45^\circ$  square lattice.

## Appendix A. Linear elasticity of the orthotropic square lattice

For an orthotropic  $\pm 45^\circ$  square lattice, we assume a state of plane stress, with the in-plane stress state written in vector form as

$$\sigma_j = (\sigma_{11}, \sigma_{22}, \sigma_{12})^T \quad (\text{A1})$$

The work-conjugate in-plane strain is also written in vector form as

$$\varepsilon_i = (\varepsilon_{11}, \varepsilon_{22}, \gamma_{12})^T \quad (\text{A2})$$

and Hooke's law reads

$$\varepsilon_i = \sum_{j=1}^3 A_{ij} \sigma_j \quad (\text{A3})$$

where the compliance matrix is of the form

$$A_{ij} = \begin{pmatrix} A_{11} & A_{12} & 0 \\ A_{12} & A_{22} & 0 \\ 0 & 0 & A_{33} \end{pmatrix} \quad (\text{A4})$$

The non-vanishing terms in Eq. (A4) are directly related to the conventional engineering moduli, such that

$$\begin{aligned} A_{11} &= 1/E_1 \\ A_{22} &= 1/E_2 \\ A_{12} &= -\nu_{21}/E_2 = -\nu_{12}/E_1 \\ A_{33} &= 1/G_{12} \end{aligned} \quad (\text{A5})$$

Classical beam theory can be used to determine the remaining four independent constants, in terms of the stockiness of the lattice  $t/l$  and the Young's modulus  $E_S$  of the solid material from which it is made. The compliance matrix of the  $\pm 45^\circ$  square lattice is given by

$$A_{ij} = \frac{1}{E_S} \begin{bmatrix} \frac{1}{2} \left(\frac{t}{l}\right) + \frac{1}{2} \left(\frac{t}{l}\right)^3 & \frac{1}{2} \left(\frac{t}{l}\right) - \frac{1}{2} \left(\frac{t}{l}\right)^3 & 0 \\ \frac{1}{2} \left(\frac{t}{l}\right) - \frac{1}{2} \left(\frac{t}{l}\right)^3 & \frac{1}{2} \left(\frac{t}{l}\right) + \frac{1}{2} \left(\frac{t}{l}\right)^3 & 0 \\ 0 & 0 & 2 \left(\frac{t}{l}\right) \end{bmatrix} \quad (\text{A6})$$

and the elastic moduli follow from Eqs. (A5) and (A6):

$$E_1 = E_2 = \frac{2(t/l)^3}{1 + (t/l)^2} E_S \quad (\text{A7})$$

$$G_{12} = \frac{1}{2} \left(\frac{t}{l}\right) E_S \quad (\text{A8})$$

$$\nu_{12} = \nu_{21} = \frac{1 - (t/l)^2}{1 + (t/l)^2} \quad (\text{A9})$$

## References

- [1] Gulati ST. Thermal stresses in ceramic wall-flow diesel filters. SAE Paper No. 830079; 1983.
- [2] Hayes RE, Kolaczkowski ST. Introduction to catalytic combustion. New York: Gordon and Breach; 1997.
- [3] Quintana-Alonso I, Fleck NA. Scripta Mater 2007;56(8):396–693.
- [4] Suo Z. J Appl Mech 1990;57:627–34.
- [5] Bao G, Ho S, Suo Z, Fan B. Int J Solids Struct 1992;29(9):1105–16.
- [6] Tada H, Paris PC, Irwin GR. The stress analysis of cracks handbook. Missouri: St. Louis; 1985.
- [7] Chakrabarty J. Theory of plasticity. Singapore: McGraw-Hill; 1987.
- [8] Huang JS, Chiang MS. Eng Fract Mech 1996;54(6):813–21.
- [9] ASTM Standard E 399. Standard test method for linear-elastic plane-strain fracture toughness  $K_{IC}$  of metallic materials; 2006.
- [10] Huang JS, Gibson LJ. Acta Metall Mater 1991;39(7):1617–26.
- [11] Sakaida Y, Tanaka K. JSME Int J Ser A 2003;46(1):30–9.
- [12] Shyam A, Lara-Curzio E, Watkins TR, Parton RJ. J Am Ceram Soc 2008;91(6):1995–2001.